J. Plasma Physics (2012), vol. 78, part 3, pp. 303–319. © Cambridge University Press 2012
doi:10.1017/S0022377812000141

Non-equilibrium modeling of the PMSE Overshoot Effect revisited: A comprehensive study

ALEXANDER BIEBRICHER[1*] and OVE HAVNES[1,2]

[1]Department of Physics and Technology, University of Tromsø, Nordlysobservatoriet, 9037 Tromsø, Norway (alexander@rocketrange.no)
[2]University Centre at Svalbard (UNIS), Pb. 156, 9171 Longyearbyen, Norway

(Received 9 June 2011; revised 12 January 2012; accepted 13 January 2012; first published online 16 February 2012)

Abstract. Numerical investigations of the Polar Mesosphere Summer Echoes (PMSE) Overshoot Effect have to date been undertaken under the premise of plasma neutrality and current equilibrium at any time. We find it necessary to revisit the calculations without these restrictions, since electrons and ions are attached to and absorbed by mesospheric dust particles at vastly different rates under PMSE conditions. We find that differences to earlier modeling might be so significant as to warrant further investigation. Furthermore, we conduct comprehensive studies of the PMSE Overshoot Effect and put the results in the context of experimental realities.

1. Introduction

The first conclusive observations of what was alternately called the 'Luminous Cirrus Cloud of June and July' [1], 'Conspicuous Phenomena in the Evening Sky' [56] or 'Sky Glows' [70] were presented by several authors in the late 19th century. These later to be renamed Noctilucent Clouds (NLC) have drawn considerable interest from the scientific community in recent decades as the number of sightings has increased (see, e.g. [2, 30, 31, 44, 55, 65, 66, 82, 108, 114] among many others).

The existence of NLC is linked to gravity wave dissipation in the mesosphere and subsequent neutral air turbulence (see, e.g. [3, 49, 72, 74, 94, 109]), which produces layers and patches of so-called dust particles or aerosols (see, e.g. [19, 36, 42, 87]). These dust particles are responsible for strong and highly aspect-sensitive radar backscatter, the Polar Mesosphere Summer Echoes (PMSE; see, e.g. [14, 23, 26, 47, 68, 76, 77, 93, 98, 107, 111] among many others).

We refer to Fritts and Alexander [29] for a review of effects of gravity waves in the mesosphere as well as to the reviews by Cho and Kelley [21], Cho and Röttger [22], Rapp and Lübken [88] or Friedrich and Rapp [28] for more information on PMSE.

A number of investigations have been conducted on the dust particles themselves (see, e.g. [8, 53, 55, 89, 91]) and it is now widely agreed upon that these mainly consist of water ice (see, e.g. [27, 43]), which crystallises on pre-existing nuclei (most likely several of these) [38] in the upper polar mesosphere during the summer months when the temperature drops from winter average values of ≈220 K to ≈130 K [73, 112]. Other suggestions include condensation on positive ion clusters [96] and homogeneous nucleation [105]. For a more detailed discussion of the microphysics of mesosphere dust particles, please see Rapp and Thomas [90].

During PMSE conditions, plasma particles, i.e. electrons or ions, may attach to dust particles so that temporally stable electron density gradients build up. Since the refractive index in the mesosphere depends, in essence, on the electron density [115], this leads to spatial fluctuations of said index and the radar beam is reflected (see, e.g. Sato [101]). The process of dust charging is thoroughly examined in a pair of papers by Weingartner and Draine [113] as well as Draine and Sutin [25].

Polar Mesosphere Summer Echoes have been observed at a wide variety of radar installations. The extrema of the appurtenant range of frequencies lie at 2.78 MHz for a radar at Tromsø, Norway [15] and 1290 MHz for the radar at Søndrestrøm, Greenland [20]. Many other observations were conducted at in-between frequencies [48, 50–52, 57, 60, 80, 97, 99].

During experiments with the European Incoherent Scatter (EISCAT) Very-High-Frequency (VHF) radar, Chilson et al. [18] found that the PMSE backscatter intensity could artificially be weakened by means of radio wave heating of the electron population in the mesosphere. This result was reproduced with the EISCAT Ultra-High-Frequency (UHF) radar by LaHoz et al. [69]. A theoretical description of the process was published by Rapp and Lübken [85], who argued that the above-mentioned electron density gradients flatten as a result of electron heating. Thus, the PMSE backscatter also recedes. Further investigations into the effectiveness of radio wave electron heating have yielded results that indicate that the heated electron temperature might, in

* Present address: Norwegian Centre for Space-related Education, P.O. Box 64, N-8483 Andenes, Norway

principle, be at a few thousand degrees Kelvin [5]. But there are practical limits that keep the heated electron temperature most likely below 1000 K [58]. More information on the theory of micro-wave-induced heating of mesospheric electrons may be found in papers by Belova et al. [5] and Kero et al. [61].

The possibility of artificially influencing the PMSE strength opens new possibilities for which new diagnostic methods and investigations have been conducted, at first by switching the heating wave on and off at equal intervals of either 10 s or 20 s length. Heating cycles of this nature mostly led to a fast mean increase of the PMSE backscatter throughout the first few cycles and saturation shortly afterward [4].

Prolonging the heater-off period leads in many cases to the appearance of the Overshoot Effect, which has been predicted by Havnes [35] and found by Havnes et al. [40]. This is called the Overshoot Effect since the PMSE backscatter, when the heating wave is switched off, may instantly become several times larger than before heating. This is due to increased dust particle charging during the heating period that leads to strong electrostatic repulsion of electrons after heating is turned off.

By far the most active site with respect to Overshoot observations has hitherto been the EISCAT site in Ramfjordmoen outside of Tromsø, Norway, where VHF and UHF radars have been used together with the EISCAT heating facility [95]. Theoretical investigations include Havnes et al. [39], Biebricher et al. [10] and Chen and Scales [16].

It has to be noted that also during winter radar backscatter can be detected. It was shown that these Polar Mesosphere Winter Echoes (PMWE) can be influenced artificially in much the same way as their summer counterparts [7, 59, 67]. Generally, the research community has begun to focus more on this phenomenon (see, e.g. [6, 12, 37, 41, 62–64, 75, 106] among many others). Zeller et al. [116] summarize the properties of PMWE on the basis of long-term observations.

The groundwork for modeling the mesosphere plasma was laid by Hill [45] who treated the problem of diffusion in weakly ionized multi-constituent plasmas. He argued that quasi-neutrality can be assumed since the electron Debye length $\lambda_{\mathrm{De}} \sim 1\,\mathrm{cm}$ is much smaller than the disturbances detected by a radar. The radar Bragg scale for $f = 50\,\mathrm{MHz}$ radar, for example, is at $\frac{\lambda}{2} \sim 3\,\mathrm{m}$. In addition, Hill [45] inferred chemical equilibrium.

The first to present a quantitative study during which plasma particle sources and sinks were not proposed to cancel each other was Reid [92], who used Natanson's electron and ion capture rates [78]. Reid concluded that several thousand icy dust particles per cubic centimeter with an average radius of $r_d \approx 10\,\mathrm{nm}$ were most likely to account for the observed electron density fluctuations. From the particle size it was then deduced that most of the dust particles should carry one negative elementary charge.

The restriction on Reid's model of singly and doubly charged dust particles was shown to be insufficient by Jensen and Thomas [54], who expanded on Reid's theory by allowing for an arbitrary negative dust particle charge.

Rapp and Lübken [86] took Jensen and Thomas' [54] studies another step further by studying not only electron but also the ion densities. They find that while the presence of dust particles unequivocally leads to electron depletions, the ion density might be locally enhanced (when recombination with electrons dominates) or decreased (when the capture by dust particles dominates) depending on the physical properties of the surrounding plasma.

The current model evolved from these studies via numerical studies by Havnes et al. [39], Biebricher et al. [10] and Scales [102].

The common denominator in the above methods is the assumption of stationary dust particles. Lie-Svendsen et al. [71] present a model which resolves this particular assumption. This last model has also been applied to the analysis of rocket data by Brattli et al. [13].

Since electrons and ions have very different masses and are absorbed by and attached to the dust at rates that differ from each other by around two orders of magnitude (see (2.3)), it becomes very probable that situations are created in which charge and flux balance might not be maintained. In other words, the present work, i.e. the examination of the Overshoot Characteristic Curve (OCC) without the constraint of plasma neutrality and ambipolar diffusion at all times, needs to be done and its results compared to earlier modeling.

In the present paper, we report from the comprehensive numerical studies of the PMSE Overshoot Effect. In Sec. 2, we introduce our model. We then choose two reference cases in Sec. 3 that are subsequently used as base plasma configurations in order to examine the OCC and the spatial and temporal development of various plasma parameters such as plasma densities, dust charge density and the plasma particle fluxes during the heating cycle in Sec. 4. In Sec. 5, we discuss the results.

2. Model

We take a dust particle layer consisting of particles of one average size to be the cause of electron and ion density variations, which in turn are responsible for fluctuations in the refractive index of the gaseous medium (see, e.g. [32, 34, 115]). Chen and Scales [16] have tested this conjecture numerically and found only 'minor differences' to the average-size case when the dust particle size was given a homogeneous or a Gaussian distribution.

In effect, we put a small Gaussian-shaped irregularity on top of what we will refer to as a 'dust cloud', i.e. a homogeneous distribution in the space of dust particles. Thus, the dust density can be written as dependent on

https://doi.org/10.1017/S0022377812000141 Published online by Cambridge University Press

spatial variable x as

$$N_{\mathrm{d}}(x) = N_{\mathrm{d0}} + hN_{\mathrm{d0}} \cdot \exp\left[-\frac{x^2}{a^2}\right]. \tag{2.1}$$

Here, N_{d} denotes the dust density with N_{d0} being the density of the dust cloud and h and a are the measures of strength and width of dust irregularity, respectively. Equation (2.1) assumes stationary dust particles.

Dust particle charging is included in the calculations following Parthasarathy [81] by assuming spherical, conducting dust particles of charge state Z and charge Ze, where e is the elementary charge. This implies that the dust particles lose or gain charge in steps of e. This makes sense with respect to charging by attachment of ions on the premise of relevant altitudes being in the transition region between two kinds of plasmas: one, where the positive particles in the plasma are heavy ion clusters, and two, where the positive particles in the plasma are lighter ions (NO^+, O_2^+). Due to the character of the positively charged species and the reactions involving them, it is highly unlikely that a dust particle gains more than one positive elementary charge at the same time through the process of ion attachment.

Therefore, an equation for the time derivative of density $N(x,Z)$ of a dust particle of charge state Z at spatial position x can be set up as follows:

$$\begin{aligned}\frac{\mathrm{d}N_{\mathrm{d}}(x,Z)}{\mathrm{d}t} &= J_{\mathrm{d}}^{i}(x,Z-1)N_{\mathrm{d}}(x,Z-1) - J_{\mathrm{d}}^{e}(x,Z)N_{\mathrm{d}}(x,Z)\\ &- J_{\mathrm{d}}^{i}(x,Z)N_{\mathrm{d}}(x,Z) + J_{\mathrm{d}}^{e}(x,Z+1)N_{\mathrm{d}}(x,Z+1)\\ &- J_{\mathrm{d}}^{\mathrm{phi}}(x,Z)N_{\mathrm{d}}(x,Z) + J_{d}^{\mathrm{phi}}(x,Z-1)N_{\mathrm{d}}(x,Z-1)\\ &- J_{\mathrm{d}}^{\mathrm{phd}}(x,Z)N_{\mathrm{d}}(x,Z) + J_{\mathrm{d}}^{\mathrm{phd}}(x,Z-1)N_{\mathrm{d}}(x,Z-1).\end{aligned} \tag{2.2}$$

$J_{\mathrm{d}}^{\mathrm{phi}}(x,Z)$ are the currents due to photo-electric effect (set to zero in the present studies) and $J_{\mathrm{d}}^{\mathrm{phd}}(x,Z) = \chi|Z|$ are the rates of electron photodetachment from dust particles [24]. $J_{\mathrm{d}}^{\mathrm{s}}(x,Z)$ are the attachment rates of plasma particles s to dust particles. These rates are defined by Draine and Sutin [25] in the form of

$$J_{\mathrm{d}}^{\mathrm{s}}(x,Z) = \tilde{J}_{\mathrm{d}}^{\mathrm{s}}(\tau,v) n_{\mathrm{s}}(x)\ \mathrm{s}_{\mathrm{s}}\pi r_{\mathrm{d}}^2 \sqrt{\frac{8k_{\mathrm{B}}T_{\mathrm{s}}}{\pi m_{\mathrm{s}}}}, \tag{2.3}$$

where $n_{\mathrm{s}}(x)$ is the density of particle species s, s_{s} is the sticking coefficient which we set to $\mathrm{s}_{\mathrm{e}} = 0.5$ and $\mathrm{s}_{\mathrm{i}} = 1$ for electrons and ions, respectively. r_{d} is the respective dust particle radius, m_{s} is the mass of the plasma particle approaching the dust particle, T_{s} its temperature and k_{B} the Boltzmann constant. The mirror image contributions $\tilde{J}_{\mathrm{d}}^{\mathrm{s}}(\tau,v)$ contain the parameter $\tau \equiv \frac{akT}{q_{\mathrm{s}}^2}$ [25] as

$$\tilde{J}_{\mathrm{d}}^{\mathrm{s}}(\tau,v) = 1 + \sqrt{\frac{\pi}{2\tau}} \tag{2.4}$$

for neutral dust particles and $v \equiv \frac{Ze}{q_{\mathrm{s}}} = 0$

$$\tilde{J}_{\mathrm{d}}^{\mathrm{s}}(\tau,v) \approx \left(1 - \frac{v}{\tau}\right)\left(1 + \sqrt{\frac{2}{\tau - 2v}}\right) \tag{2.5}$$

for $v < 0$, i.e. an attractive Coulomb potential at distance from the dust particle and

$$\tilde{J}_{\mathrm{d}}^{\mathrm{s}}(\tau,v) \approx \left(1 + \frac{1}{\sqrt{4\tau + 3v}}\right)^2 e^{-\frac{\Theta_v}{\tau}} \tag{2.6}$$

for $v > 0$, i.e. a repulsive far-distance Coulomb potential. Θ_v in (2.6) is a dimensionless measure of the potential maximum, which we set here as equal to zero.

The plasma particle densities are taken into account with the help of continuity equations by Jensen and Thomas [54] in the non-steady state form,

$$\begin{aligned}\frac{\partial}{\partial t}n_e(x) + \frac{\partial}{\partial x}(n_e(x)v_e(x)) &= Q + Q_{\mathrm{p}} - \alpha_{ei}n_e(x)\ n_i(x)\\ &- D^{-}(x,Z)n_e(x),\end{aligned} \tag{2.7}$$

$$\begin{aligned}\frac{\partial}{\partial \mathrm{t}}n_i(x) + \frac{\partial}{\partial x}(n_i(x)v_i(x)) &= Q - \alpha_{ei}n_e(x)\ n_i(x)\\ &- D^{+}(x,Z)n_i(x),\end{aligned} \tag{2.8}$$

where the coefficient of dissociative recombination for plasma particle species s is $\alpha_{ei} = 2.1 \times 10^{-7}\sqrt{\frac{300}{T_i}}$ [11]. Q is the ion–electron pair production rate, Q_{p} is the photo-emission rate, v_{s} is the fluid velocity of particle species s and $D^{\pm}$ are the loss rates of plasma particles to the dust.

In addition, we use the collisional equation of motion for plasma particle species s:

$$\begin{aligned}m_{\mathrm{s}}n_{\mathrm{s}}(x)\frac{\mathrm{d}v_{\mathrm{s}}(x)}{\mathrm{d}t} &= m_{\mathrm{s}}n_{\mathrm{s}}(x)\left[\frac{\partial v_{\mathrm{s}}(x)}{\partial t} + \left(v_{\mathrm{s}}(x)\frac{\partial}{\partial x}\right)v_{\mathrm{s}}(x)\right]\\ &= q_{\mathrm{s}}n_{\mathrm{s}}(x)\ E(x) - k_{\mathrm{B}}T_{\mathrm{s}}\frac{\partial}{\partial x}n_{\mathrm{s}}(x) - m_{\mathrm{s}}n_{\mathrm{s}}(x)v_{\mathrm{s}}v_{\mathrm{s}}(x).\end{aligned} \tag{2.9}$$

Here, m_{s}, q_{s}, n_{s}, v_{s} and T_{s} are the mass, charge, number density, fluid velocities and temperatures of electron and ions, respectively. E is the electric field, k_{B} is the Boltzmann constant and ν_{s} is the frequency of collisions between respective plasma and neutral air particles.

We define the frequency of this collision following Hill and Bowhill [46] as

$$\begin{aligned}\nu_{\mathrm{s}} \equiv\ & 2.6 \cdot 10^{-9} n_{\mathrm{n}} \times\ 0.78\frac{28}{\tilde{m}_{\mathrm{s}} + 28}\sqrt{1.74\frac{\tilde{m}_{\mathrm{s}} + 28}{28\tilde{m}_{\mathrm{s}}}}\\ &+ 2.6 \times\ 10^{-9} n_{\mathrm{n}} \times\ 0.21\frac{32}{\tilde{m}_{\mathrm{s}} + 32}\sqrt{1.57\frac{\tilde{m}_{\mathrm{s}} + 32}{32\tilde{m}_{\mathrm{s}}}}\\ &+ 2.6 \cdot 10^{-9} n_{\mathrm{n}} \times\ 0.01\frac{40}{\tilde{m}_{\mathrm{s}} + 40}\sqrt{1.64\frac{\tilde{m}_{\mathrm{s}} + 40}{40\tilde{m}_{s}}},\end{aligned} \tag{2.10}$$

where $n_n = 2.3 \cdot 10^{14}\,\mathrm{cm}^{-3}$ is the number density of neutral particles and $\tilde{m}_{\mathrm{s}} \equiv \frac{m_{\mathrm{s}}}{m_{\mathrm{u}}}$.

Please note that there is no magnetic field contribution in (2.9). This has its reason in the Earth's magnetic field being nearly vertical in the polar mesosphere, i.e. it lines up with spatial dimension in modeling to a sufficiently good degree.

https://doi.org/10.1017/S0022377812000141 Published online by Cambridge University Press

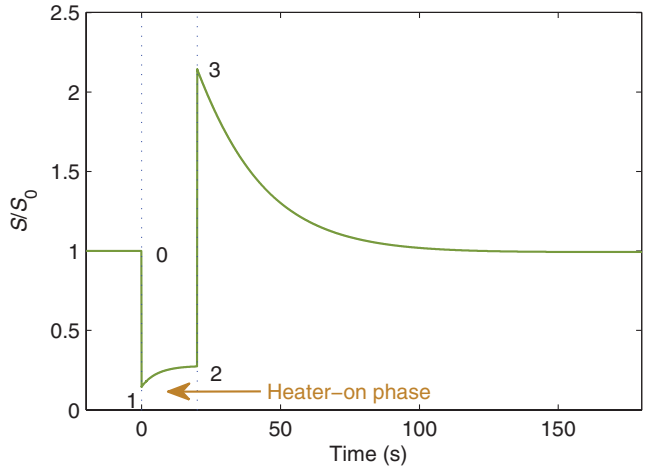

Figure 1. (Colour online) Shape of the classical OCC.

We employ Poisson's equation,

$$\frac{\partial}{\partial x}E(x) = \frac{e}{\varepsilon}\left(n_{\mathrm{i}}(x) - n_{\mathrm{e}}(x) + \sum_{Z} N_{\mathrm{d}}(x, Z)Z\right). \tag{2.11}$$

Here, q is the elementary charge, ε is the dielectric constant of the medium, Z is the charge state of the respective dust particle and N_{d} is the dust particle number density.

The simulation is then run (with initially uncharged dust particles) to find the quasi-steady state for a given plasma before time analysis starts: the heating cycle is structured as shown in Fig. 1. The heating is turned on at $t = 0\,\mathrm{s}$ (point 0) and kept for $\Delta t_{\mathrm{heating}} = 20\,\mathrm{s}$ (from point 1 to point 2) after which the plasma is given time to relax for $\Delta t_{\mathrm{relax}} = 160\,\mathrm{s}$ (from point 3). During the simulation run on temporal (t) and spatial (x) information, mainly the following plasma parameters are obtained:

- Electron and ion density $n_{\mathrm{e}}(t, x)$, $n_{\mathrm{i}}(t, x)$,
- dust particle charge state distribution $N_{\mathrm{d}}(t, x, Z)$ and dust particle charge density $c_{\mathrm{d}}(t, x) = \sum_Z N_{\mathrm{d}}(x, Z)Z$,
- electric field $E(t, x)$,
- electron and ion fluid velocities $v_{\mathrm{e}}(t, x)$, $v_{\mathrm{i}}(t, x)$.

Fluid velocities and plasma particle densities can be combined to find plasma fluxes and the spatial electron density distribution is ultimately used to calculate the effective backscatter intensity S as,

$$S \propto |\Delta\mathscr{N}_{\mathrm{e}}(K)|^2 S_{\mathrm{init}}, \tag{2.12}$$

where S_{init} is the intensity of the radar wave before scattering and $\Delta\mathscr{N}_{\mathrm{e}}(K)$ is the one-dimensional spatial Fourier transformation of the electron density gradient $\Delta n_{\mathrm{e}}(x)$. For the derivation of (2.12) we refer to Nygren [79].

Even though there are many estimates (see, e.g. [32, 47, 87, 100]), there are still difficulties in putting any computed value of radar reflectivity and backscatter intensity into experimental perspective, which is why we focus here on relative values of the radar backscatter.

3. Computational details

Experimentally, it was originally found that the dust particle sizes responsible for PMSE can vary from 10–20 nm with densities of up to an order of magnitude of $\sim 1000\,\mathrm{cm}^{-3}$ to optically observable sizes of $\geqslant 20{-}30\,\mathrm{nm}$ with densities of an order of magnitude of $\sim 100\,\mathrm{cm}^{-3}$ [110]. We consider two dust sizes of $r_{\mathrm{d1}} = 10\,\mathrm{nm}$ and $r_{\mathrm{d2}} = 30\,\mathrm{nm}$ with corresponding dust particle densities $N_{\mathrm{d0,1}} = 200\,\mathrm{cm}^{-3}$ and $N_{\mathrm{d0,2}} = 80\,\mathrm{cm}^{-3}$.

The relative height h of the dust peak described in (2.1) is chosen to be 0.1. In this way, the study looks at both smaller dust irregularities of, for example, $1\,\mathrm{cm}^{-3}$ in absolute height at $N_{\mathrm{d0}} = 10\,\mathrm{cm}^{-3}$ and larger irregularities of $55\,\mathrm{cm}^{-3}$ in absolute height at $N_{\mathrm{d0}} = 550\,\mathrm{cm}^{-3}$.

Values for the ion–electron pair production rate Q can vary strongly from $\sim 10^{-3}\,\mathrm{cm}^{-3}$ (quiet nighttime conditions) to $\sim 10^{3}\,\mathrm{cm}^{-3}\,\mathrm{s}^{-1}$ (disturbed daytime conditions) [83]. Since such stark variation also results in very different PMSE backscatter intensity and shapes of the OCC, we adopt a Q-value that corresponds to quiet daytime conditions.

With respect to the temperatures used for reference cases, we point to several studies that put the unheated or cold plasma particle temperature at 130–150 K (see, e.g. [33, 73, 112]). We use $T_{\mathrm{ep}} = 130\,\mathrm{K}$. We choose the heated electron temperature to be $T_{\mathrm{eh}} = 500\,\mathrm{K}$.

The photo-detachment strength is set to $\chi = 0.01$. It is to be noted in this respect that Dimant and Milikh [24] and Rapp [84] assert photo-detachment to be of importance in the summer mesosphere, whereas Havnes et al. [39] dispute this on the basis of experimental evidence. They set an upper limit of $\chi \leqslant 0.03$. We hold that $\chi = 0.01$ does not significantly alter our results.

Lastly, the altitude range in question implies an ion mass $m_{\mathrm{i}} = 50\ \ m_{\mathrm{u}}$, where m_{u} is the atomic mass. In accordance with Reid [92] (see also Lie-Svendsen et al. [71]) we adopt this weight to represent the average weight of a singly and positively charged plasma particle species in model calculations.

In summary, the reference plasma RP_1 for smaller dust particles is as follows:

- Dust particle density: $N_{\mathrm{d0,1}} = 200\,\mathrm{cm}^{-3}$,
- dust particle radius: $r_{\mathrm{d1}} = 10\,\mathrm{nm}$.

The reference plasma RP_2 for bigger dust particles is as follows:

- Dust particle density: $N_{\mathrm{d0,2}} = 80\,\mathrm{cm}^{-3}$,
- dust particle radius: $r_{\mathrm{d2}} = 30\,\mathrm{nm}$.

Common for both reference plasmas are

- ion–electron pair production rate: $Q = 10\,\mathrm{cm}^{-3}\,\mathrm{s}^{-1}$,
- cold plasma temperature: $T_{\mathrm{ep}} = 130\,\mathrm{K}$,
- heated electron temperature: $T_{\mathrm{eh}} = 500\,\mathrm{K}$,
- relative height of the dust peak: $h = 0.1$.

https://doi.org/10.1017/S0022377812000141 Published online by Cambridge University Press

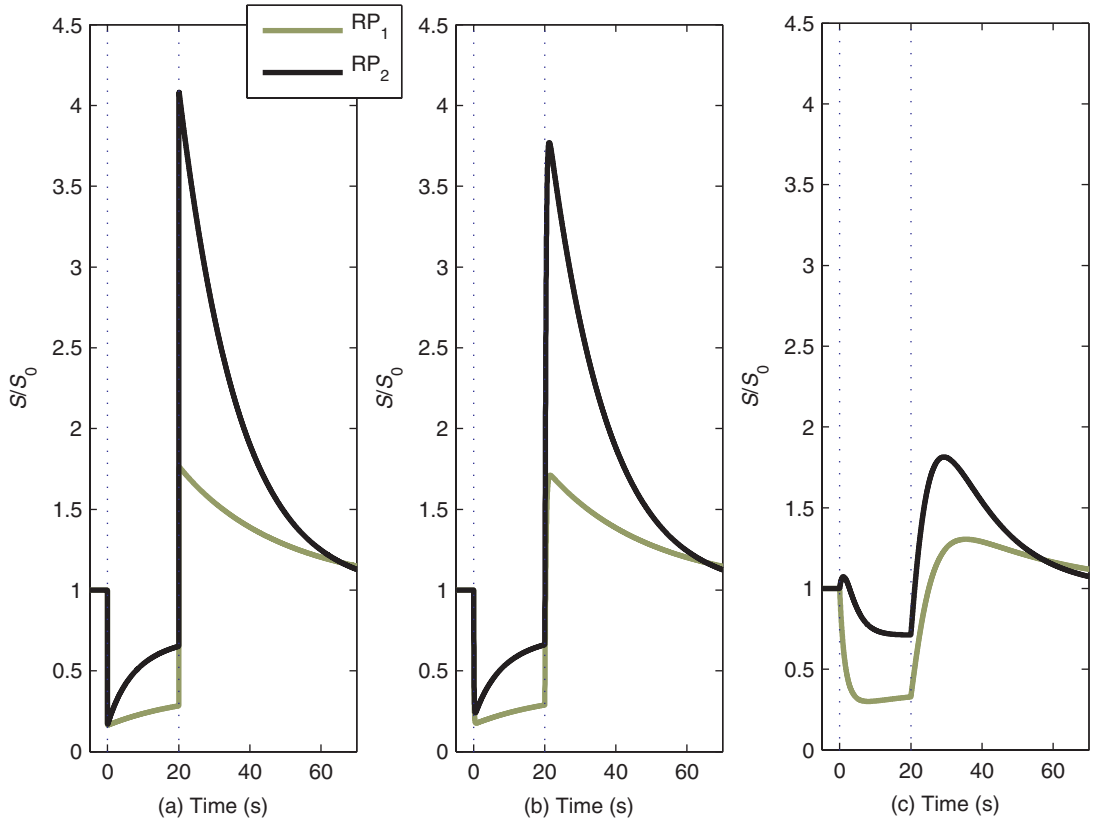

Figure 2. (Colour online) Overshoot characteristic curves for reference cases as described in Sec. 3. Panels (a)–(c) denote UHF, VHF and MORRO radar frequencies, respectively. The green lines denote RP_1, while the black lines denote RP_2.

Different plasma parameters, such as electron and ion densities and velocities, as well as the dust charge density and the electric field, can then be calculated at different and relevant radar frequencies. Figure 2 shows the results. Panel (a) denotes the case of the EISCAT UHF radar with a frequency, $f_{\mathrm{UHF}} = 929\,\mathrm{MHz}$, which corresponds to a Bragg scale for the coherent backscatter of $\frac{\lambda}{2} = 0.16\,\mathrm{m}$. Panel (b) denotes the EISCAT VHF-radar ($f_{\mathrm{VHF}} = 224\,\mathrm{MHz}$, $\frac{\lambda}{2} = 0.67\,\mathrm{m}$) and panel (c) denotes the MORRO-radar at the EISCAT site ($f_{\mathrm{MORRO}} = 56\,\mathrm{MHz}$, $\frac{\lambda}{2} = 2.67\,\mathrm{m}$). The Bragg scale is then set into (2.1) as parameter a.

It is evident from the figure that the two chosen reference plasmas result in a case of rather moderate (RP_1) and a case of strong Overshoot (RP_2). They serve as a starting point for the numerical analysis that follows.

4. Results

4.1. Plasma parameters in comparison to earlier modeling

Examples of spatial and temporal plasma parameter distributions have been presented by Lie-Svendsen et al. [71], Biebricher et al. [10] and in a series of papers by Scales and Chen [16, 17, 102–104], but no comprehensive analysis of plasma densities and fluxes has been performed as yet to the best of our knowledge.

Figure 3 lays down the possible shapes of spatial distributions of different plasma parameters for reference plasma RP_1 as defined in Sec. 3. The values are taken at time $t = 0$, directly before heating is switched on. Here, the altitude is measured in units of the Bragg length $\frac{\lambda}{2}$ of the respective radar. Panel (a) demonstrates how the electron depletion deforms at longer radar wavelengths. Lie-Svendsen et al. [71] find asymmetries in both electron and ion density distributions, which are related to their approach of a dust density irregularity moving through a particular altitude range by means of gravity and dust diffusion processes. Since we here consider the dust particles to be stationary, we do not reproduce this asymmetry.

We secure the values of n_{e}, n_{i} and c_{d} in Fig. 4 at spatial postion $x = 0$, where, due to the symmetry inherent in our approach, the net plasma movement is equal to zero.

The top row of Fig. 4 discloses the equilibrium electron density at spatial position $x = 0$ in dependence on background dust density N_{d0} (panel (a)) and ion–electron pair production rate Q (panel (b)) for both reference plasmas RP_1 and RP_2 and all three radar frequencies. The results are consistent with the findings of Biebricher et al. [10] that the more dust particles are present, the more electrons are trapped on the surfaces of these particles or absorbed into their bulk mass such that the electron density decreases.

Panel (b) in Fig. 4 displays how the electron density changes when different values of the ion–electron pair production rate Q are entered into the simulation. Higher Q corresponds to more electrons and ions in the dust cloud. However, as the dust cloud has

https://doi.org/10.1017/S0022377812000141 Published online by Cambridge University Press

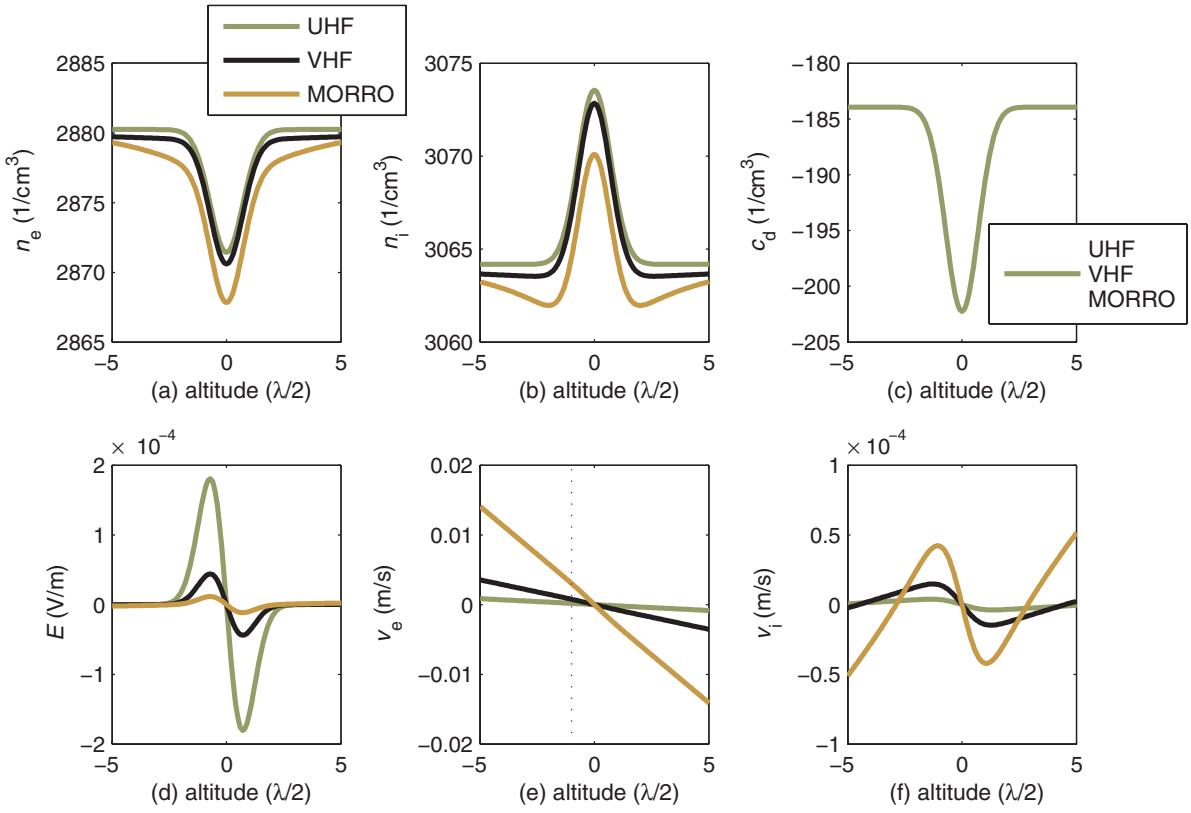

Figure 3. (Colour online) Examples of plasma parameter distributions with respect to altitude for reference plasma RP_1 as defined in Sec. 3. Different colors indicate three radar frequencies: $f_{UHF} = 929\,MHz$ (green), $f_{VHF} = 224\,MHz$ (black) and $f_{MORRO} = 56\,MHz$ (ochre). In panel (c), shapes of different radar frequencies are indistinguishable. The y-axis labels denote the respective plasma parameters with their corresponding units given in square brackets.

a limited capacity of capturing charged particles, the general development is toward a saturation value $Q_{sat} = \alpha n_{e,sat} n_{i,sat}$.

The ion density results in the second row are based on the same calculations as in the top row of the same figure. The proportionality factors in the linear development of ion densities are smaller than those of electron densities, which is due to the presence of negatively charged dust particles. The more dust particles are present, the larger is the difference between ion and electron densities such that the ion density necessarily decreases slower than the electron density with increasing N_{d0} [10].

The third row of Fig. 4 quantifies the split in electron and ion densities in terms of the background dust density N_{d0} and the ion–electron pair production rate Q. The linear dependence of the split on the dust density is weaker by a factor of almost 10 in proportionality factor in reference plasma RP_2.

We also give the results of the computations for the dust charge density c_d in the bottom row of Fig. 4.

Figure 5 shows examples of how different plasma parameters may react during temperature changes inherent in the heating cycle. The spatial positions used here are $x = 0$ for the top row and $x = -\frac{\lambda}{2}$ in the bottom row variables. The electron density (panel (a)) reacts to the enhancement of the electron temperature with increased electron attachment to the surface of the dust particles, thus charging them more negatively. In addition, absorption of the plasma particles into the bulk mass of dust particles, i.e. particle loss, increases as well. Thus, the electron density in the centre of the dust cloud decreases slowly during the heating period. Accordingly, the dust particle charge density c_d (panel (c)) develops toward more negative values. The ion density is governed by the electron and dust charge densities via Poisson's equation (2.11) and increases. It is interesting to note that the ion density reacts with the temperature change with a discontinuity which is visible in some cases. This is not consistent with the findings of Biebricher et al. [10] and a direct consequence of introducing finite streaming velocities: The diffusion term in (2.8) dominates to such a degree that the ion density is most dependent on the flux into the dust cloud. Therefore, the discontinuity in ion density mirrors the discontinuity in ion fluid velocity v_i (panel (f)). Since in the case of electrons absorption and attachment are much more important, the discontinuity does not show in the figure. Its magnitude is generally less than 0.1% of the change in electron density during the heating phase.

In the top row of Fig. 6, the ratio in electron density at points 2 and 0 in dependence on background dust

https://doi.org/10.1017/S0022377812000141 Published online by Cambridge University Press

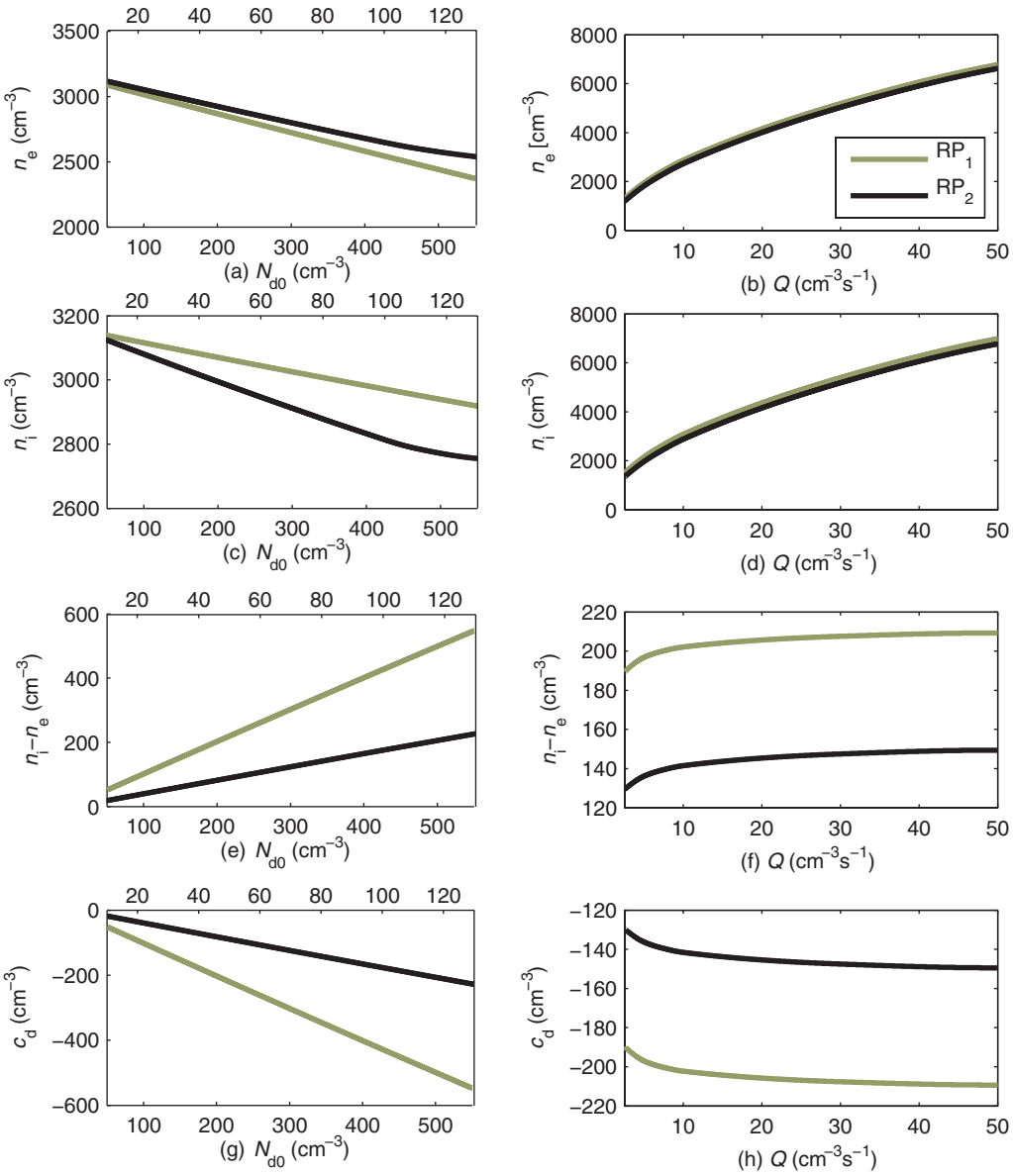

Figure 4. (Colour online) Plasma densities in dependence on background dust density N_{d0} (left column) and ion–electron pair production rate Q (right column). The values for all three radar frequencies lie within 1% at all values of N_{d0} and Q. Reference plasmas RP_1 (bottom axis in the left column) and RP_2 (top axis in the left column) are marked by green and black colors, respectively.

density N_{d0} (left column), ion–electron pair production rate Q (middle column) and heated electron temperature T_{eh} (right column) is presented.

In panel (a), the ratio $n_e(2)/n_e(0)$ is depicted for reference plasma RP_1 (green, bottom axis) and reference plasma RP_2 (black, top axis). In the case of the UHF radar frequency and reference plasma RP_2 (solid black line), the value of $N_{d0} = 130\,\mathrm{cm}^{-3}$ is larger than expected. As the dust density grows, the ion attachment and absorption may, in fact, be significant in the UHF case. Thus, the de-charging of dust particles may be more effective than otherwise.

Panel (b) in Fig. 6 displays the dependency of $n_e(2)/n_e(0)$ on the ion–electron pair production rate Q. As $Q \to \infty$, $n_e(2)/n_e(0) \to 1 - \epsilon$ ($\epsilon > 0, \epsilon \ll 1$), i.e. a value close to but not quite equal to 1.

The saturation value of $n_e(2)/n_e(0)$ in dependence with the heated electron temperature T_{eh} is determined by the most negative charge $Z_{min}e$ that the respective dust particles can carry. As a practical matter, of course, Z_{min} is not reached in all the particles of a large assembly of dust particles due to a multitude of charging and de-charging processes happening at all times in model simulations and, more so, in the Earth's atmosphere.

For the sake of completeness, we also show the dust charge density ratio $c_d(2)/c_d(0)$ in the bottom row of Fig. 6.

https://doi.org/10.1017/S0022377812000141 Published online by Cambridge University Press

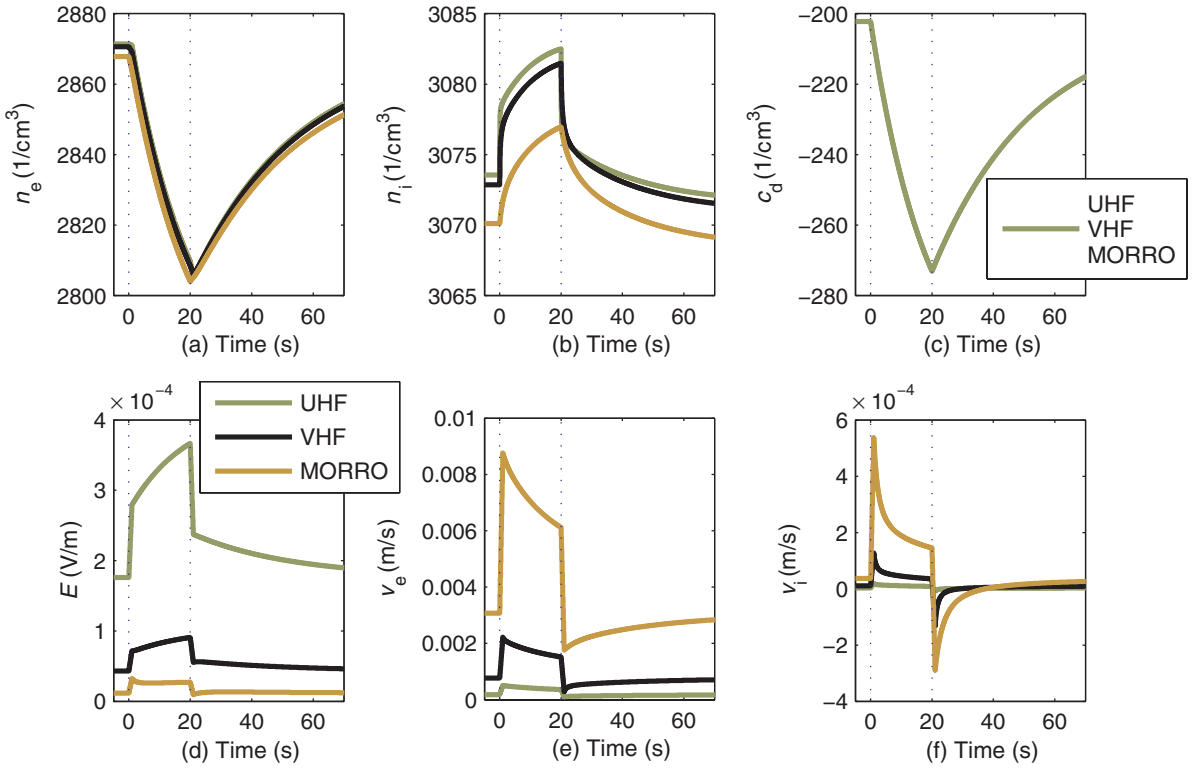

Figure 5. (Colour online) Examples of plasma parameter time evolution graphs in reference plasma RP_1 as defined in Sec. 3. The vertical dotted lines indicate the period during which the heater wave is switched on. In panel (c), the graphs for the three radar frequencies are indistinguishable. For all other panels, the legend in panel (d) is valid.

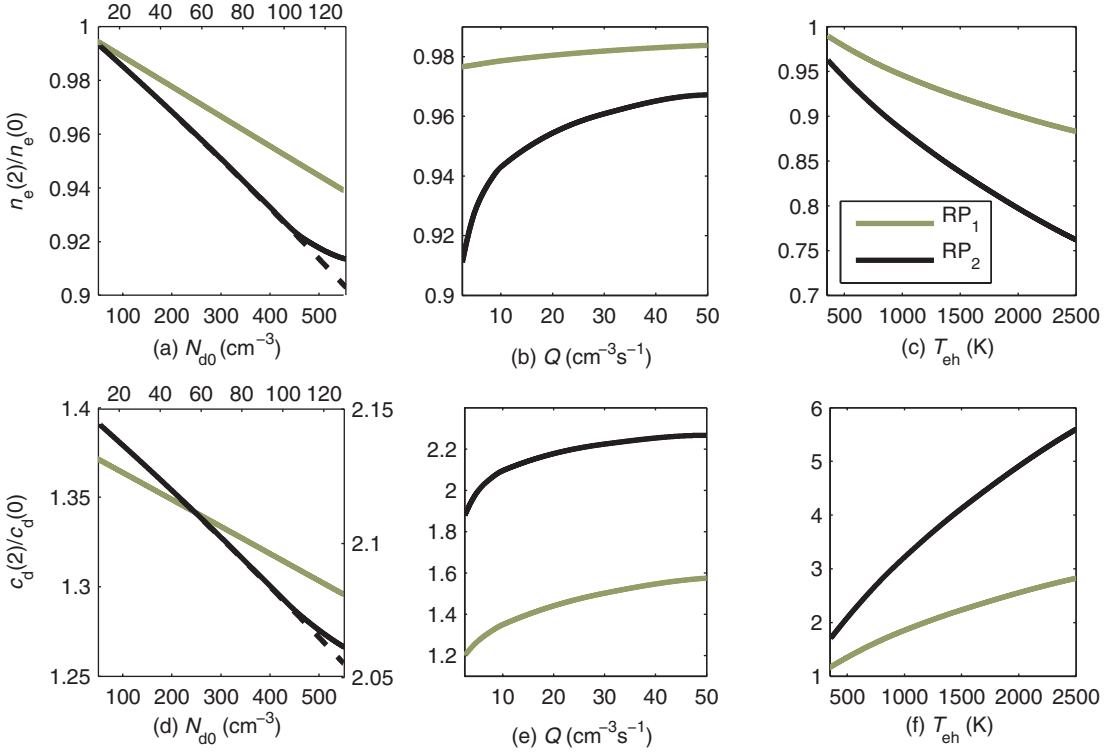

Figure 6. (Colour online) Ratio of electron density (top row) and dust charge density (bottom row) at points 2 and 0 as defined in Fig. 1 in dependence on background dust density N_{d0} (left column), ion–electron pair production rate Q (middle column) and heated electron temperature T_{eh} (right column). Values for reference plasmas RP_1 and RP_2 are given in green and black colors, respectively. In the left column, the top and right axes denote RP_2 while the bottom and left axes denote RP_1. In this column, the dashed, black lines indicate the VHF and MORRO radar frequencies while the solid, black line indicates the UHF frequency. All lines denote both UHF, VHF and MORRO frequency. Please note different y-axis scales in panel (d).

https://doi.org/10.1017/S0022377812000141 Published online by Cambridge University Press

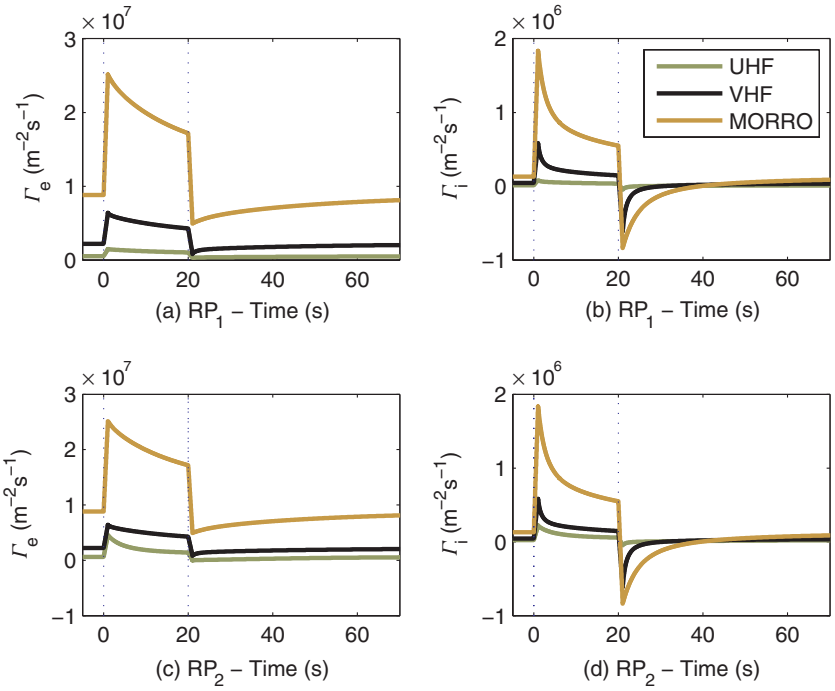

Figure 7. (Colour online) Examples of temporal progression through the heating cycle of electron and ion fluxes Γ_e (left column) and Γ_i (right column). In the top row, the developments of reference plasma RP_1 as defined in Sec. 3 are displayed while the values for reference plasma RP_2 are found in the bottom row. The colors denote the plasma frequencies (see legend in panel (b)).

4.2. *Plasma streaming*

Electron and ion flux are defined as

$$\Gamma_s = n_s v_s, \tag{4.1}$$

where n_s and v_s are the number density and fluid velocity of plasma particle species s. Figure 7 shows examples of how electron and ion fluxes, Γ_e and Γ_i, behave during the heating cycle.

The flux enhancement as the heater is turned on at $t = 0$ is very distinct, as is the reaction to switching the heater off. In fact, the sudden repulsion of electrons from the dust cloud when heating is turned off necessarily leads to a discontinuity in both the electron and ion fluxes.

Since in our setup the fluxes are both equal to zero at spatial position $x = 0$, we use the values at $x = -\frac{\lambda}{2}$ in the following discussion.

Figure 8 displays the ratio $\frac{\Gamma_i}{\Gamma_e}$ depending on the background dust density N_{d0} (top row) and ion–electron pair production rate Q (bottom row) directly before heating is switched on. RP_1 and RP_2 are denoted by the line colors as given in the legend in panel (f). It is seen that this ratio is generally of order of magnitude ∼0.01, i.e. the electron flux is by about two orders of magnitude larger than the ion flux.

Increasing N_{d0} leads to decreasing $\frac{\Gamma_i}{\Gamma_e}$. This is due to the fact that electron attachment and absorption increase more strongly with dust density than ion attachment and absorption by the dust particles.

There is an exception to this. At UHF frequency, $\frac{\Gamma_i}{\Gamma_e}$ increases disproportionally at larger dust densities. This development is most pronounced in RP_2 and is based on the small diffusion times at this particular frequency. If, in addition, streaming is enhanced either by the presence of more and/or bigger dust particles, a situation may be created where ion absorption by and attachment to dust particles is no longer negligible. The ion flux may, in fact, come within 10% of the electron flux. Panels (a) and (c) in Fig. 4 reflect this in the form of enhanced number densities of both electrons and ions at high densities.

Increasing the number density of electrons and ions in plasma via larger Q values leads to a similar development. The ratio $\frac{\Gamma_i}{\Gamma_e}$ increases toward a saturation value when $Q \to \infty$.

One of the major results of this paper, which is discussed in more detail in Sec. 5, is based on the results presented in Fig. 9. Here, the same ratio as in Fig. 8 is given directly after switching on the heating wave. It is seen that the ratio $\frac{\Gamma_i}{\Gamma_e}$ becomes very different when heating is switched on. With earlier models, which assumed ambipolar streaming, i.e. quasi-neutrality at all times in plasma, this cannot be reproduced.

When heating is switched on, the charging of dust particles changes as, depending on the effectiveness of the heater wave, many more electrons are absorbed and attached to dust particles. The electron flow Γ_e increases accordingly but not as much as the ion flow Γ_i. As mentioned above, the ion flow is, in a relative sense, more dependent on change in electron temperature, as it is mainly facilitated by electrostatic attraction, which in turn depends on the electric field in the dust cloud

https://doi.org/10.1017/S0022377812000141 Published online by Cambridge University Press

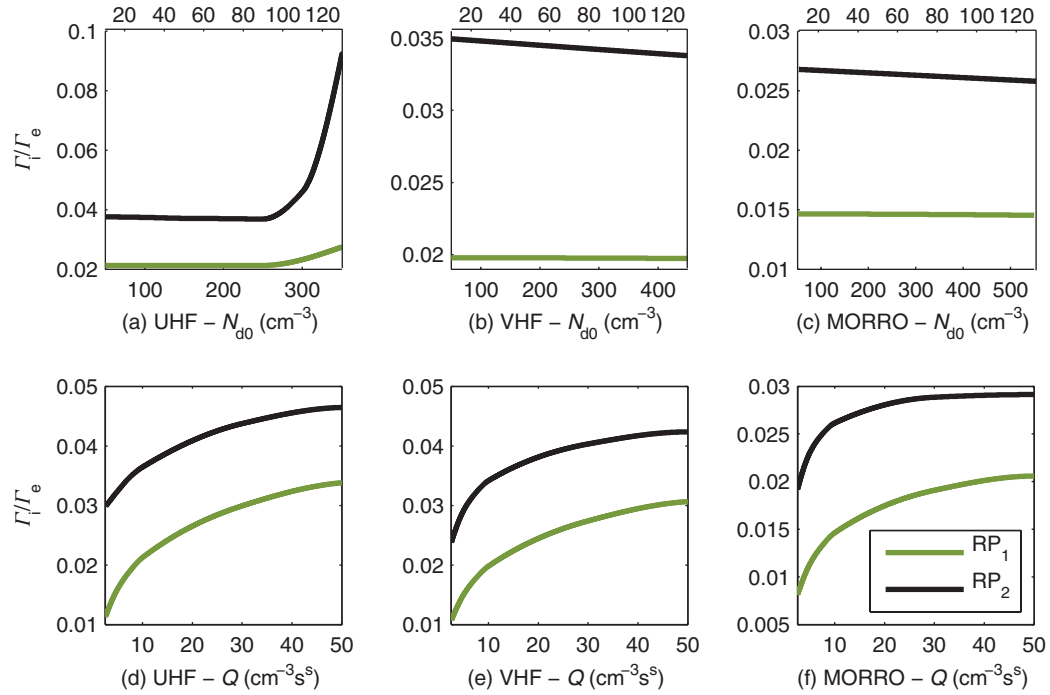

Figure 8. (Colour online) Flux ratio $\frac{\Gamma_i}{\Gamma_e}$ at point 0, i.e. right *before* heating is switched on, in dependence on background dust particle density N_{d0} (top row) and ion–electron pair production rate Q (bottom row). The respective radar frequencies are given in the x-labels of the panels while the colors denote RP_1 and RP_2 according to the legend in panel (f).

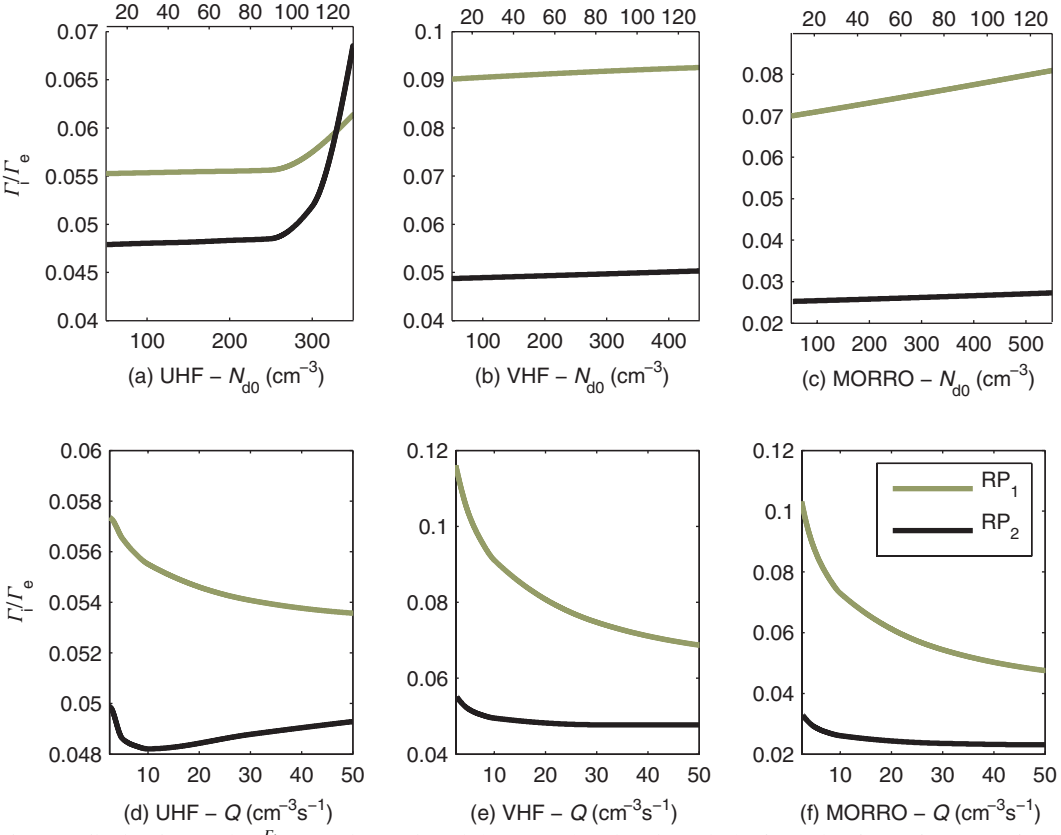

Figure 9. (Colour online) Flux ratio $\frac{\Gamma_i}{\Gamma_e}$ at point 1, i.e. right *after* heating is switched on, in dependence on background dust particle density N_{d0} (top row) and ion–electron pair production rate Q (bottom row). The respective radar frequencies are given in the x-labels of the panels while colors denote RP_1 and RP_2 according to the legend in panel (f).

https://doi.org/10.1017/S0022377812000141 Published online by Cambridge University Press

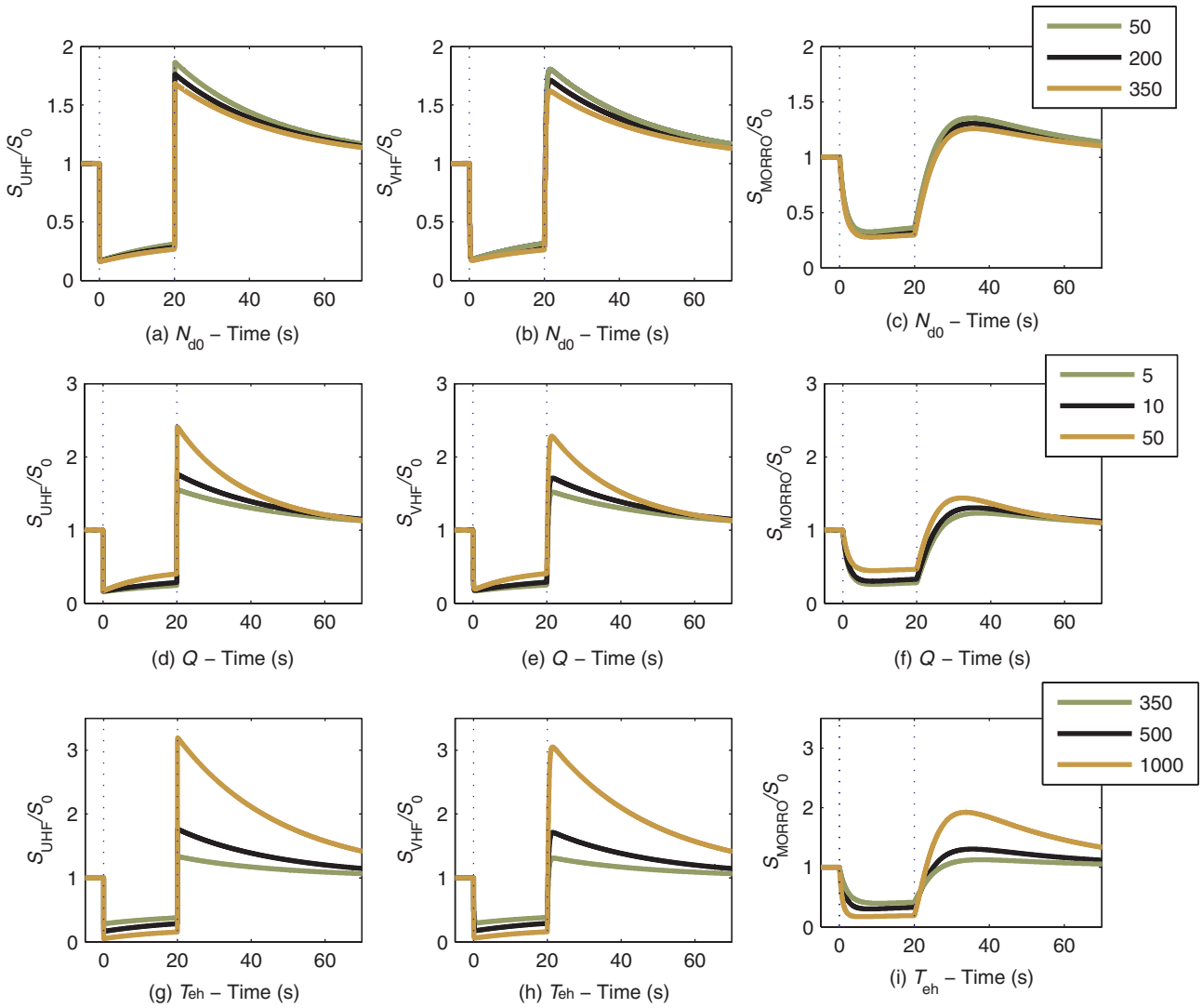

Figure 10. (Colour online) Overshoot Characteristic Curve calculated in reference plasma RP_1 as defined in Sec. 3. The top row denotes varying background dust particle density N_{d0}, the middle row varying ion–electron pair production rate Q and the bottom row varying heated electron temperature T_{eh}. Values in the legends are given in units as $[N_{d0}] = 1\,\mathrm{cm}^{-3}$, $[Q] = 1\,\mathrm{cm}^{-3}\,\mathrm{s}^{-1}$ and $[T_{eh}] = 1\,\mathrm{K}$, respectively. The left column shows radar frequency $f_{UHF} = 929\,\mathrm{MHz}$, the middle column $f_{VHF} = 224\,\mathrm{MHz}$ and the right column $f_{MORRO} = 56\,\mathrm{MHz}$.

(see Fig. 5). The electron flow is mainly driven by the electron density gradient, which changes on a slower time scale than the electric field.

An interesting aspect of the figure is that the tendencies of the flux ratio with increasing background dust density N_{d0} and ion–electron pair production rate Q are generally opposite when after-heating is compared to before-heating. This too is a token of the fact that the electric field reacts almost instantaneously to the temperature change, while the reduction in electron density happens over a longer time scale.

4.3. Overshoot Characteristic Curves

The plasma parameter developments outlined in Sec. 4.1 translate into different shapes of OCC. Figure 10 displays selected examples of OCC, which belong to the calculations made in RP_1. The figure is structured such that the columns denote different radar frequencies and the rows are defined by their varying plasma parameters, the background dust density N_{d0} in panels (a)–(c), the ion–electron pair production rate Q in panels (d)–(f) and the heated electron temperature T_{eh} in panels (g)–(i). The normalization value S_0 refers to the respective PMSE intensity at point 0 of the heating cycle, i.e. just before the heating wave is switched on.

General tendencies for change in OCC shape due to different plasma parameters, which have already been identified by Havnes et al. [39] and Biebricher et al. [10], are still valid: higher dust density leads to stronger plasma particle absorption, which diminishes the Overshoot Effect. Higher ion–electron pair production rate has the opposite effect as stronger ionization in the plasma leads to increased electron density in the dust cloud and with it to increased charging of dust particles.

https://doi.org/10.1017/S0022377812000141 Published online by Cambridge University Press

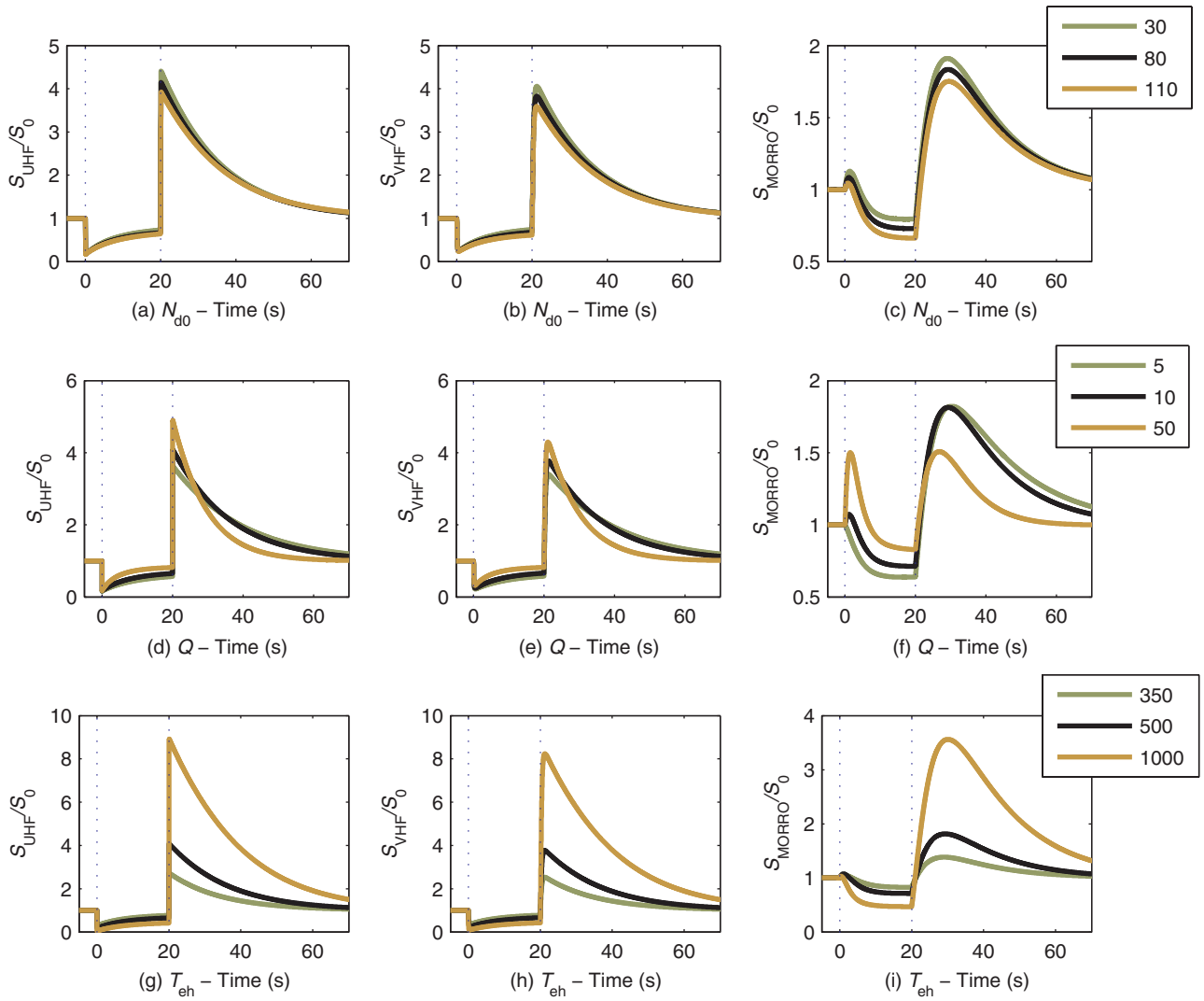

Figure 11. (Colour online) OCC calculated in reference plasma RP_2 as defined in Sec. 3. The top row denotes varying background dust particle density N_{d0}, the middle row varying ion–electron pair production rate Q and the bottom row varying heated electron temperature T_{eh}. The values of the units are as follows: $[N_{d0}] = 1\,cm^{-3}$, $[Q] = 1\,cm^{-3}\,s^{-1}$ and $[T_{eh}] = 1\,K$. The left column denotes a radar frequency, $f_{UHF} = 929\,MHz$, the middle column denotes $f_{VHF} = 224\,MHz$ and the right column denotes $f_{MORRO} = 56\,MHz$. Please note the changed axis labels for the MORRO figures.

The only difference is that when plasma is replenished into the dust cloud on a finite time scale, absorption processes cannot dominate over electron attachment when the heated temperatures are $T_{eh} > 1000\,K$. In other words, while Biebricher et al. [10] found a time delay in maximum backscatter after heating is turned off for high T_{eh}, we here do not find such a time delay based on dominating plasma particle absorption by the dust but rather as a consequence of finite diffusion times and to a significant degree only at the frequency of the MORRO radar.

In Fig. 11, where the OCC of the calculations in reference plasma RP_2 are displayed in the same structure as before, all developments become more pronounced. The larger grain radius aids attachment of electrons to dust particles to a point where the Turn-on Overshoot is found in most of the OCC at MORRO frequency. Generally, the TOO ratio $\frac{S_{TOO}}{S_0}$ does not exceed ≈ 1.50 but rather stays significantly smaller than that with $\frac{S_{TOO}}{S_0} \leqslant 1.1$.

Note that the difference in Overshoot ratio between the UHF and VHF frequencies, which could exceed 10%, was reproduced with an instantaneous-diffusion model [9].

For further discussion, we can point to Fig. 12 where OCC are displayed in dependence on the radar Bragg scale. $\frac{\lambda}{2}$ increases from darker to lighter colors from $\frac{\lambda}{2} = 0.16\,m$ to $\frac{\lambda}{2} = 10\,m$. The panels (a)–(d) denote a dust particle radius, $r_d = 10\,nm$, 30 nm, 50 nm and 70 nm, respectively. For small PMSE dust particles, $r_d = 10\,nm$, there is only very weak TOO for the widest dust particle irregularity. Even though the electron attachment increases for the larger dust particles, there is generally no TOO for $\frac{\lambda}{2} < 2.67\,m$, i.e. at the Bragg scale of the MORRO radar, TOO is found for particles of larger size than $r_d \geqslant 30\,nm$.

https://doi.org/10.1017/S0022377812000141 Published online by Cambridge University Press

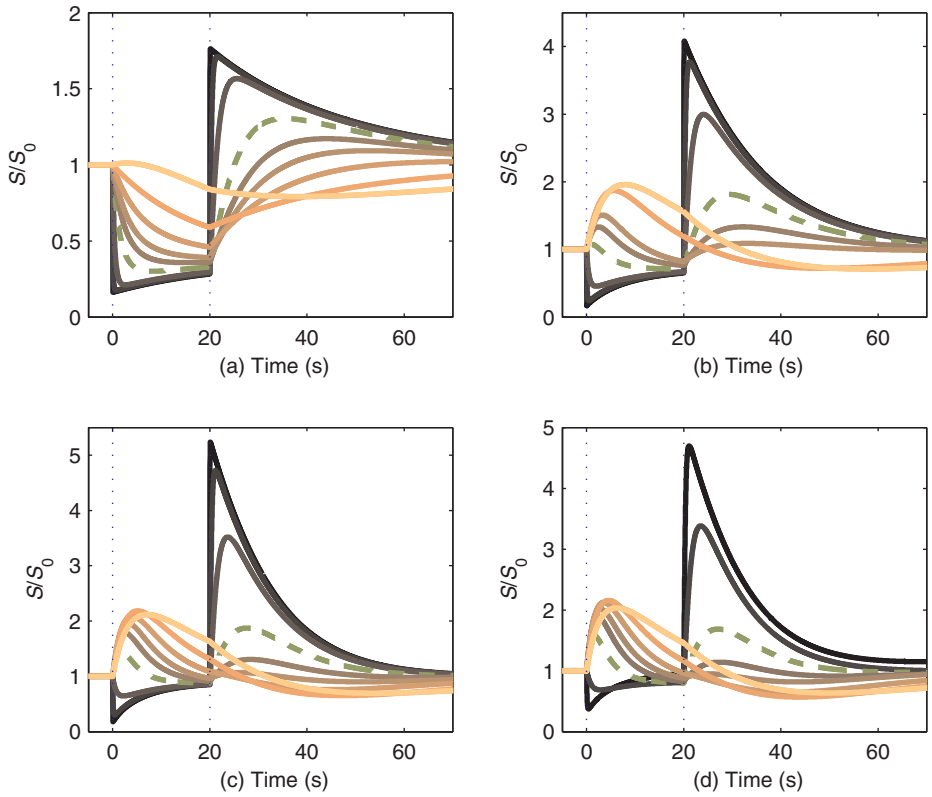

Figure 12. (Colour online) OCC shapes for different sizes of the radar Bragg length. From darker to lighter color, the Bragg length used in the calculations changes from $\frac{\lambda}{2} = 0.16\,\mathrm{m}$ to $\frac{\lambda}{2} = 10\,\mathrm{m}$. a: Dust particle radius $r_\mathrm{d} = 10\,\mathrm{nm}$ (RP_1). b: Dust particle radius $r_\mathrm{d} = 30\,\mathrm{nm}$ (RP_2). c: Dust particle radius $r_\mathrm{d} = 50\,\mathrm{nm}$. d: Dust particle radius $r_\mathrm{d} = 70\,\mathrm{nm}$. The MORRO-OCC for all four cases is highlighted by the dashed, green lines.

5. Discussion

In the present paper, the results of comprehensive numerical studies of the PMSE Overshoot Effect are presented and compared with earlier modeling. Different plasma parameters, such as electron and ion densities, as well as dust charge density, electron and ion flux are analyzed in terms of their dependence on dust particle density and size, ion–electron pair production rate and heated electron temperature and their reaction to artificial heating. Generally, the agreement of newer and earlier modeling results is good, albeit not unequivocally so.

The main assumption made by earlier modeling is that at any given time the plasma is quasi-neutral. In this way, (2.7) can be replaced by the simple relation,

$$n_\mathrm{e}(x) = n_\mathrm{i}(x) + c_\mathrm{d}(x). \tag{5.1}$$

A direct consequence of the system of equations which is set up thus, is that ambipolar diffusion can be assumed such that the electric field is readily obtained from current equilibrium.

The premise of said assumption is that the Debye length in the plasma is much smaller than the Bragg length of the radars involved. Our 'kitchen-sink' approach to modeling the Overshoot Effect is partly motivated by the idea that the Debye length is a 'local' quantity derived from the electric field around one plasma particle whereas our problem is 'global' in the sense that we look at an assembly of many particles in the form of a dust cloud with ambient electrons and ions. On the global scale, electric fields are not uncommon in a plasma. For example, an electromagnetic wave in a plasma would not exist without the presence of an electric field. In the case of our dust cloud where both ions and electrons are absorbed by and attached to dust particles at significantly different rates and the dust density is varying with space, the buildup of a global electric field is necessary to counteract plasma production and recombination processes. Thus, quasi-neutrality of the plasma is principally violated from the get-go and the question rather becomes whether the assumption of quasi-neutrality is good enough for the purpose of the respective studies. We do not intend to give an answer to this particular question, nor indeed could we. But it is worth mentioning that our results indicate, at least, that quasi-neutrality should be investigated further in the context of a study of the Overshoot Effect. We base this assertion on the differences that we find in electron and ion streaming directly before and after heating. As a case study, we can point to the computational results found by Chen and Scales [16], who used the above assumption in their modeling of OCC. A re-calculation of their results with their model and using our model (with the same parameters) leads

https://doi.org/10.1017/S0022377812000141 Published online by Cambridge University Press

to the following: Calculations with the earlier model yield larger recombination rates, or stronger charging directly before and after the heating changes such that stronger changes in backscatter are found than in the calculations with the present model.

In the mold of this argument, a prediction about the occurrence of the Turn-on Overshoot Effect in experiments has to be revisited. Chen and Scales [16] hypothesize that this should be possible as they predict the Turn-on Overshoot at 'near or below 50 MHz' radar frequency [16], which is a frequency close to the MORRO frequency. We principally agree, but want to add a caveat in that, the Turn-on Overshoot, in our calculations, has a tendency to occur only when the dust particle charging processes are enhanced via high ionization in the plasma or bigger dust particles. Strong source processes denote a high level of ionization in the plasma, which, it is reasonable, to assume extends lower into the mesosphere, i.e. below the PMSE layer. Thus, following a line of thought presented by Kassa et al. [58], a significant part of the heating wave might be absorbed before it reaches PMSE heights thereby decreasing the effect of heating on PMSE electrons and the chance for an observable OCC. When the particle size is increased and the Q-value is held at $Q = 10\ \mathrm{cm^3 s^{-1}}$, such as in Fig. 12, strong TOO of $\frac{S_{\mathrm{TOO}}}{S_0} > 1.5$ shows only at radar frequencies significantly smaller than $f_{\mathrm{MORRO}} = 56\,\mathrm{MHz}$ in our calculations.

Acknowledgements

All numerical data have been obtained via computations at the supercomputing facilities of the Computer Center at the University of Tromsø, Norway.

References

[1] Backhouse, T. W. 1885 The luminous cirrus cloud of June and July. *Meteorol. Mag.* **20**, 133.

[2] Balsiger, F., Kopp, E., Friedrich, M., Torkar, K. M., Wälchli, U. and Witt, G. 1996 Positive ion depletion in a noctilucent cloud. *Geophys. Res. Lett.* **23**, 93–96.

[3] Balsley, B. B., Ecklund, W. L. and Fritts, D. C. 1983 VHF echoes from high-latitude mesosphere and lower thermosphere observations and interpretations. *J. Atmos. Sci.* **40**, 2451.

[4] Belova, E., Chilson, P., Kirkwood, S. and Rietveld, M. T. 2003 The response time of PMSE to ionospheric heating. *J. Geophys. Res.* **108**, 8446.

[5] Belova, E. G., Pashin, A. B. and Lyatsky, W. B. 1995 Passage of powerful HF radio wave through the ionosphere as a function of initial electron density profiles. *J. Atmos. Terr. Phys.* **57**, 265–272.

[6] Belova, E., Kirkwood, S., Ekeberg, J., Osepian, A., Häggström, I., Nilsson, H. and Rietveld, M. T. 2005 The dynamical background of polar mesosphere winter echoes from simultaneous EISCAT and ESRAD observations. *Ann. Geophys.* **23**, 1239.

[7] Belova, E., Smirnova, M., Rietveld, M. T., Isham, B., Kirkwood, S. and Sirgienko, T. 2008 First observation of the overshoot effect for polar mesospheric winter echoes during radiowave electron temperature modulation. *Geophys. Res. Lett.* **35**, L03110.

[8] Berger, U. and Von Zahn, U. 2002 Icy particles in the summer mesopause region: 3-d modelling of their environment and 2-d modelling of their transport. *J. Geophys. Res.* **107**, 1366.

[9] Biebricher, A., Havnes, O. and Bast, R. 2011 On the necessary complexity of modeling of the Polar Mesosphere Summer Echo Overshoot Effect. *J. Plasma Phys.* **78**, 225–239.

[10] Biebricher, A., Havnes, O., Hartquist, T. W. and LaHoz, C. 2006 On the influence of plasma absorption by dust on the PMSE overshoot effect. *Adv. Space. Res.* **38**, 2541–2550.

[11] Brasseur, G. and Solomon, S. 1995 *Aeronomy of the Middle Atmosphere*. Dordrecht, Netherlands: D. Reidel.

[12] Brattli, A., Blix. T. A., Lie-Svendsen, Ø., Hoppe, U.-P., Lübken, F.-J., Rapp, M., Singer, W., Latteck, R. and Friedrich, M. 2006 Rocket measurements of positive ions during polar mesosphere winter echo conditions. *Atmos. Chem. Phys.* **6**, 5515.

[13] Brattli, A., Lie-Svendsen, Ø., Svenes, K., Hoppe, U.-P., Strelnikova, I., Rapp, M., Latteck, R. and Friedrich, M. 2009 The ECOMA 2007 campaign: rocket observations and numerical modelling of aerosol particle charging and plasma depletion in a PMSE/NLC layer. *Ann. Geophys.* **27**, 781–796.

[14] Bremer, J., Hoffmann, P., Latteck, R. and Singer, W. 2003 Seasonal and long-term variation of PMSE from VHF radar observations at Andenes, Norway. *J. Geophys. Res.* **108**, (D8)8438.

[15] Bremer, J., Hoffmann, P., Manson, A., Meek, C., Rüster, R. and Singer, W. 1996 PMSE observations at three different frequencies in northern Europe during summer 1994. *Ann. Geophys.* **14**, 1317–1327.

[16] Chen, C. and Scales, W. A. 2005 Electron temperature enhancement effects on plasma irregularities associated with charged dust in the Earth's mesosphere. *J. Geophys. Res.* **110**, A12313 (13 pp).

[17] Chen, C. and Scales, W. A. 2007 Active perturbation of dust-associated electron irregularities in the earth's mesosphere: discrete-charging effects. *IEEE Trans. Plasma Sci.* **35**, 731–735.

[18] Chilson, P. B., Belova, E., Rietveld, M. T., Kirkwood, S. and Hoppe U. P. 2000 First artificially induced modulation of PMSE using the EISCAT heating facility. *Geophys. Res. Lett.* **27**, 3801.

[19] Cho, J. Y. N., Alcala, C. M., Kelley, M. C. and Swartz, W. E. 1996 Further effects of charged aerosols on summer mesospheric radar scatter. *J. Atmos. Terr. Phys.* **58**, 661.

[20] Cho, J. Y. N. and Kelley, M. C. 1992 Enhancement of Thomson scatter by charged aerosols in the polar mesosphere: measurements with a 1.29 GHz radar. *Geophys. Res. Lett.* **19**, 1097–1100.

[21] Cho, J. Y. N. and Kelley, M. C. 1993 Polar mesosphere summer radar echoes. *Rev. Geophys.* **31**, 243–265.

[22] Cho, J. Y. N. and Röttger, J. 1997 An updated review of polar mesospheric summer echoes: observations, theory and their relationship to noctilucent clouds and subvisible aerosols. *J. Geophys. Res.* **102**, 2001.

[23] Czechowsky, P., Reid, I. M., Rüster, R. and Schmidt, G. 1989 VHF radar echoes observed in the summer and winter polar mesosphere over Andøya, Norway. *J. Geophys. Res.* **94**, 5199.

[24] Dimant, Y. S. and Milikh, G. M. 2004 Effect of radio wave heating on polar mesospheric clouds. *Adv. Space. Res.* **34**(11), 2413.

[25] Draine, B. T. and Sutin, B. 1987 Collisional charging of interstellar grains. *Astrophys. J.* **320**, 803.

[26] Ecklund, W. L. and Balsley, B. B. 1981 Long-term observations of the Arctic mesosphere with the MST radar at Poker Flat, Alaska. *J. Geophys. Res.* **86**, 7775.

[27] Eremenko, M. N., Petelina, S. V., Zasetsky, A. Y., Karlsson, B., Rinsland, C. P., Llewellyn, E. J. and Sloan, J. J. 2005 Shape and composition of PMC particles derived from satellite remote sensing measurements. *Geophys. Res. Lett.* **32**, L16S06.

[28] Friedrich, M. and Rapp, M. 2009 News from the lower ionosphere: a review of recent developments. *Surv. Geophys.* **30**, 525–559.

[29] Fritts, D. C. and Alexander, M. J. 2003 Gravity wave dynamics and effects in the middle atmosphere. *Rev. Geophys.* **41**, 1003.

[30] Gadsden, M. and Schröder, W. 2003 *Noctilucent Clouds*. New York: Springer Verlag.

[31] Garcia, R. R. 1989 Dynamics, radiation, and photochemistry in the mesosphere: implications for the formation of noctilucent clouds. *J. Geophys. Res.* **94**, 14605–14615.

[32] Ginsburg, V. L. 1964 *The Propagation of Electromagnetic Waves in Plasmas*. Oxford, UK: Pergamon Press.

[33] Hale, B. N. and Plummer, P. L. M. 1974 Molecular model for ice clusters in supersaturated vapor. *J. Chem. Phys.* **61**, 4012.

[34] Hargreaves, J. K. 1992 *The Solar-Terrestrial Environment. An Introduction to Geospace – The Science of the Terrestrial Upper Atmosphere, Ionosphere and Magnetosphere*. Cambridge, UK: Cambridge University Press.

[35] Havnes, O. 2004 Polar Mesospheric Summer Echoes (PMSE) overshoot effect due to cycling of artificial electron heating. *J. Geophys. Res.* **109**(A2), 1–7.

[36] Havnes, O., Brattli, A., Aslaksen, T., Singer, W., Latteck, R., Blix, T., Thrane, E. and Trøim, J. 2001 First common-volume observations of layered plasma structures and polar mesospheric echoes by rocket and radar. *Geophys. Res. Lett.* **28**, 1419.

[37] Havnes, O. and Kassa M. 2009 On the sizes and observable effects of dust particles in polar mesospheric winter echoes. *J. Geophys. Res.* **114**, D09209, 11 pp.

[38] Havnes, O. and Næsheim, L. I. 2007 On the secondary charging effects and structure of mesospheric dust particles impacting rocket probes. *Ann. Geophys.* **25**, 623.

[39] Havnes, O., LaHoz, C., Biebricher, A., Kassa, M., Meseret, T., Næsheim, L. I. and Zivkovic, T. 2004 Investigation of the mesospheric PMSE conditions by use of the new overshoot effect. *Phys. Scr.* **T107**, 70.

[40] Havnes, O., LaHoz, C., Næsheim, L. I. and Rietveld, M. T. 2003 First observations of the PMSE overshoot effect and its use for investigating the conditions in the summer mesosphere. *Geophys. Res. Lett.* **30**, 2229.

[41] Havnes, O., LaHoz, C., Rietveld, M. T., Kassa, M., Baroni, G. and Biebricher, A. 2009 *Observation and Analysis of Polar Mesospheric Winter Echoes Modulated by Artificial Electron Heating*. Washington, DC: ESA Publication.

[42] Havnes, O., Melandsø, F., LaHoz, C., Aslaksen, T. K. and Hartquist, T. W. 1992 Charged dust in the Earth's mesopause, effects on radar backscatter. *Phys. Scr.* **45**, 535.

[43] Hervig, M., Thompson, R., McHugh, M., Gordley, L., Russell III, J. and Summers, M. 2001 First confirmation that water ice is the primary component of polar mesospheric clouds. *Geophys. Res. Lett.* **28**, 971–974.

[44] Hesstvedt, E. 1961 Note on the nature of noctilucent clouds. *J. Geophys. Res.* **66**, 1985–1987.

[45] Hill, R. J. 1978 Non-neutral and quasi-neutral diffusion of weakly ionized multi-constituent plasma. *J. Geophys. Res.* **83**, 989–998.

[46] Hill, R. J. and Bowhill, S. A. 1977 Collision frequencies for use in the continuum momentum equations applied to the lower ionosphere. *J. Atmos. Terr. Phys.* **39**, 803.

[47] Hocking, W. K. and Röttger, J. 1983 Studies of polar mesosphere summer echoes over EISCAT using calibrated signal strengths and statistical parameters. *Radio Sci.* **18**, 1312.

[48] Hocking, W. K. and Röttger, J. 1997 Pulse-length dependence of radar signal strengths for Fresnel backscatter. *Radio Sci.* **32**, 1425.

[49] Holton, J. R. 1982 The role of gravity wave-induced drag and diffusion in the momentum budget of the mesosphere. *J. Atmos. Sci.* **39**, 791–799.

[50] Hoppe, U.-P., Hall, C. and Röttger, J. 1988 First observations of summer polar mesospheric backscatter with a 224 MHz radar. *Geophys. Res. Lett.* **15**, 28–31.

[51] Huaman, M. M., Kelley, M. C., Hocking, W. K. and Woodman, R. F. 2001 Polar mesosphere summer echo studies at 51.5 MHz at Resolute Bay, Canada: comparison with Poker Flat results. *Radio Sci.* **36**, 1823–1837.

[52] Inhester, B., Ulwick, J., Cho, J. Y. N., Kelley, M. and Schmidt, G. 1990 Consistency of rocket and radar electron density observations: implications about the anisotropy of turbulence. *J. Atmos. Terr. Phys.* **52**, 855–873.

[53] Jensen, E. and Thomas, G. E. 1988 A growth-sedimentation model of polar mesospheric clouds: comparisons with SME measurements. *J. Geophys. Res.* **93**, 2461–2473.

[54] Jensen, E. and Thomas, G. E. 1991 Charging of mesospheric particles: implications of electron density and particle coagulation. *J. Geophys. Res.* **96**, 18603.

[55] Jensen, E., Thomas, G. E. and Toon, O. B. 1989 On the diurnal variation of noctilucent clouds. *J. Geophys. Res.* **94**, 14693–14702.

[56] Jesse, O. 1885 Auffallende Erscheinungen am Abendhimmel. *Met. Zeit.* **2**, 311–312.

[57] Karashtin, A. N., Shlyugaev, Y. V., Abramov, V. I., Belov, I. F., Berezin, I. V., Bychkov, V. V., Eryshev, E. B. and Komrakov, G. P. 1997 First HF radar measurements of summer mesopause echoes at SURA. *Ann. Geophys.* **15**, 935–941.

[58] Kassa, M., Havnes, O. and Belova, E. 2005 The effect of electron bite-outs on artificial electron heating and PMSE overshoot. *Ann. Geophys.* **23**, 3633.

[59] Kavanagh, A., Honary, F., Rietveld, M. T. and Senior, A. 2006 First observations of the artificial modulation of polar mesospheric winter echoes. *Geophys. Res. Lett.* **33**, L19801.

[60] Kelley, M. C., Huaman, M., Chen, C. Y., Ramos, C., Djuth, F. and Kennedy, E. 2002 Polar mesosphere summer observations at HF frequencies using the HAARP Gakona Ionospheric Observatory. *Geophys. Res. Lett.***29**(12), 44-1–44-4.

[61] Kero, A., Bösinger, T., Pollari, P., Turunen, E. and Rietveld, M. 2000 First EISCAT measurements of electron-gas temperature in the artificially heated D-region ionosphere. *Ann. Geophys.* **18**, 1210–1215.

[62] Kero, A., Enell, C. F., Kavanagh, A. J., Vierinen, J., Virtanen, I. and Turunen, E. 2008 Could negative ion production explain the polar mesosphere winter echo (PMWE) modulation in active HF heating experiments? *Geophys. Res. Lett.* **35**, 23.

[63] Kirkwood, S., Barabash, V., Belova, E., Nilsson, H., Rao, T. N., Stebel, K., Osepian, A. and Chilson, P. B. 2002 Polar mesosphere winter echoes during solar proton events. *Adv. Polar Upper Atmos. Res.* **16**, 111.

[64] Kirkwood, S., Chilson, P., Belova, E., Dalin, P., Häggström, I., Rietveld, M. T. and Singer, W. 2006 Infrasound – the cause of strong polar mesosphere winter echoes? *Ann. Geophys.* **24**, 475.

[65] Klostermeyer, J. 1998 A simple model of the ice particle size distribution in noctilucent clouds. *J. Geophys. Res.* **103**, 28743–28752.

[66] Kopp, E., Eberhardt, P., Herrmann, U. and Björn, L. G. 1985 Positive ion composition of the high latitude summer D-region with noctilucent clouds. *J. Geophys. Res.* **90**, 13041–13051.

[67] La Hoz, C. and Havnes, O. 2008 Artificial modification of polar mesospheric winter echoes with an RF heater: do charged dust particles play an active role? *J. Geophys. Res.* **113**, D19205.

[68] LaHoz, C., Havnes, O., Næsheim, L. I. and Hysell, D. L. 2006 Observations and theories of polar mesospheric summer echoes at a Bragg wavelength of 16 cm. *J. Geophys. Res.* **111**, D04203.

[69] LaHoz, C., Næsheim, L. I., Havnes, O. and Rietveld, M. T. 2003 First observation of the artificial electron heating induced reduction of the PMSE strength at 933 MHz. In: *Proceedings of the EISCAT Workshop*, Menlo Park, USA, August 14–19.

[70] Leslie, R. J. 1885 Sky glows. *Nature* **33**, 245.

[71] Lie-Svendsen, Ø., Blix, T. A., Hoppe, U.-P. and Thrane, E. V. 2003 Modeling the plasma response to small-scale aerosol particle perturbations in the mesopause region. *J. Geophys. Res.* **108**, 8442.

[72] Lindzen, R. S. and Holton, J. R. 1981 A theory of the quasi-bieninial oscillation. *J. Atmos. Sci.* **25**, 1095.

[73] Lübken, F.-J. 1999 Thermal structure of the Arctic summer mesosphere. *J. Geophys. Res.* **104**, 9135.

[74] Lübken, F.-J., Lehmacher, G., Blix, T. A., Hoppe, U.-P., Thrane, E., Cho, J. and Swartz, W. 1993 First in-situ observations of neutral and plasma density fluctuations within a PMSE layer. *Geophys. Res. Lett.* **20**, 2311–2314.

[75] Lübken, F.-J., Strelnikov, B., Rapp, M., Singer, W., Latteck, R., Brattli, A., Hoppe, U.-P. and Friedrich, M. 2006 The thermal and dynamical state of the atmosphere during polar mesospheric winter echoes. *Atmos. Chem. Phys.* **6**, 13.

[76] Morris, R. J., Murphy, D. J., Reid, I. M., Holdsworth, D. A. and Vincent, R. A. 1991 First polar mesosphere summer echoes observed at Davis, Antarctica (68.6° S). *J. Geophys. Res.* **96**, 5837.

[77] Næsheim, L. I., Havnes, O. and LaHoz, C. 2008 A comparison of polar mesosphere summer echo at VHF (224 MHz) and UHF (930 MHz) and the effects of artificial electron heating. *J. Geophys. Res.* **113**, D08205.

[78] Natanson, G. L. 1960 On the theory of the charging of amicroscopic aerosol particles as a result of capture of gas ions. *Sov. Phys. Tech. Phys.* **5**, 538–551.

[79] Nygren, T. 1996 *Introduction to Incoherent Scatter Measurements*. Sodankylä, Finland: Invers Oy.

[80] Ogawa, T., Arnold, N. F., Kirkwood, S., Nishitani, N. and Lester, M. 2003 Finnland HF and Esrange MST radar observations of polar mesosphere summer echoes. *Ann. Geophys.* **21**, 1047–1055.

[81] Parthasarathy, P. 1976 Mesopause dust as a sink for ionization. *J. Geophys. Res.* **81**, 2392.

[82] Plane, J. M. C. 2000 The role of sodium bicarbonate in the nucleation of noctilucent clouds. *Ann. Geophys.* **18**, 807–814.

[83] Rapp, M. 2000 Aerosol layers in the polar summer mesosphere: interaction with the plasma of the D-region and dependence on temperature and dynamics. *Doctoral thesis*, Bonn University, Germany.

[84] Rapp, M. 2009 Charging of mesospheric aerosol particles: the role of photo detachment and photoionization from meteoric smoke and ice particles. *Ann. Geophys.* **27**, 2417–2422.

[85] Rapp, M. and Lübken, F.-J. 2000 Electron temperature control of PMSE. *Geophys. Res. Lett.* **27**, 3285.

[86] Rapp, M. and Lübken, F.-J. 2001 Modelling of particle charging in the polar mesosphere: Part 1 – general results. *J. Atmos. Sol. Terr. Phys.* **63**, 759.

[87] Rapp, M. and Lübken, F.-J. 2003 On the nature of PMSE: electron diffusion in the vicinity of charged particles revisited. *J. Geophys. Res.* **108**, 8437.

[88] Rapp, M. and Lübken, F.-J. 2004 Polar mesosphere summer echoes (PMSE): review of observations and current understanding. *Atmos. Chem. Phys.* **4**, 2601.

[89] Rapp, M., Lübken, F.-J., Müllemann, A., Thomas, G. E. and Jensen, E. 2002 Small-scale temperature variations in the vicinity of NLC: experimental and model results. *J. Geophys. Res.* **107**, 4392.

[90] Rapp, M. and Thomas, G. E. 2006 Modeling of the microphysics of mesospheric ice particles: assessment of current capabilities and basic sensitivities. *J. Atmos. Sol. Terr. Phys.* **68**, 715–744.

[91] Reid, G. C. 1975 Ice clouds at the summer polar mesopause. *J. Atmos. Sci.* **32**, 523–535.

[92] Reid, G. C. 1990 Ice particles and electron 'bite-outs' at the summer polar mesopause. *J. Geophys. Res.* **95**, 13891–13896.

[93] Reid, I. M., Czechowsky, P., Rüster, R. and Schmidt, G. 1989 First VHF radar measurements of mesopause summer echoes at mid-latitudes. *Geophys. Res. Lett.* **16**, 135.

[94] Reid, I. M., Rüster, R. and Schmidt, G. 1987 VHF radar observations of cat's eye-like structures at mesospheric heights. *Nature* **327**, 43.

[95] Rietveld, M. T., Kohl, H. K. and Kopka, H. 1993 Introduction to ionospheric heating at Tromsø. Part I: Experimental overview. *J. Atmos. Terr. Phys.* **55**, 577.

[96] Robertson, S., Horányi, M., Knappmiller, S., Sternovsky, Z., Holzworth, R., Shimogawa, M., Friedrich, M., Torkar, K., Gumbel, J., Megner, L., et al. 2009 Mass analysis of charged aerosol particles in NLC and PMSE during the ECOMA/MASS campaign. *Ann. Geophys.* **27**, 1213.

[97] Röttger, J. 2001 Observations of the polar D-region and the mesosphere with the EISCAT Svalbard radar and the SOUSY Svalbard radar. *Mem. Nat. Inst. Pol. Res.* **54**, 9–20.

[98] Röttger, J., LaHoz, C., Kelley, M. C., Hoppe, U.-P. and Hall, C. 1988 The structure and dynamics of polar mesosphere summer echoes observed with the EISCAT 224 MHz radar. *Geophys. Res. Lett.* **15**, 1353–1356.

[99] Röttger, J., Rietveld, M. T., LaHoz, C., Hall, C., Kelley, M. C. and Swartz, W. 1990 Polar mesosphere summer echoes observed with the EISCAT 933-MHz radar and the CUPRI 46.9-MHz radar, their similarity to 224-MHz radar echoes and their relation to turbulence and electron density profiles. *Radio Sci.* **25**, 671–687.

[100] Røyrvik, O. and Smith, L. G. 1984 Comparison of mesospheric VHF radar echoes and rocket probe electron concentration measurements. *J. Geophys. Res.* **89**, 9014.

[101] Sato, T. 1989 Radar principles. In: *Handbook for MAP*, Vol. 30 (ed. S. Fukao). Urbana, IL: SCOSTEP, 19 pp.

[102] Scales, W. A. 2004 Electron temperature effects on small-scale plasma irregularities associated with charged dust in the earths mesosphere. *IEEE Trans. Plasma Sci.* **32**, 724.

[103] Scales, W. A. and Chen, C. 2008 On initial enhancement of mesospheric dust associated plasma irregularities subsequent to radiowave heating. *Ann. Geophys.* **26**, 2265–2271.

[104] Scales, W. A. and Chen, C. 2008 On the initial perturbation of mesospheric dust associated irregularities by high-powered radio waves. *Adv. Space Res.* **41**(1), 50–56.

[105] Shimizu, S., Klumov, B., Shimizu, T., Rothermel, H., Havnes, O., Thomas, H. M. and Morfill, G. E. 2010 Synthesis of water ice particles in a plasma chamber. *J. Geophys. Res.* **115**, D18205.

[106] Stebel, K., Blum, U., Fricke, K.-H., Kirkwood, S., Mitchell, N. J. and Osepian, A. 2004 Joint radar/lidar observations of possible aerosol layers in the winter mesosphere. *J. Atmos. Sol. Terr. Phys.* **66**, 957.

[107] Thomas, L., Astin, I. and Prichard, I. T. 1992 The characteristics of VHF echoes from the summer mesopause region and mid-latitudes. *J. Atmos. Terr. Phys.* **54**, 969.

[108] Turco, R. P., Toon, O. B., Whitten, R. C., Keesee, R. G. and Hollenbach, D. 1982 Noctilucent clouds: simulation studies of their genesis, properties and global influences. *Planet. Space Sci.* **3**, 1147–1181.

[109] Vincent, R. A. and Reid, I. M. 1983 HF doppler measurements of mesospheric momentum fluxes. *J. Atmos. Sci.* **40**, 1321–1333.

[110] von Cossart, G., Fiedler J. and Von Zahn, U. 1999 Size distributions of NLC particles as determined from 3-color observations of NLC by ground-based lidar. *Geophys. Res. Lett.* **26**, 1513.

[111] Von Zahn, U. and Bremer, J. 1999 Simultaneous and common-volume observations of noctilucent clouds and polar mesosphere summer echoes. *Geophys. Res. Lett.* **26**, 1521.

[112] von Zahn, U. and Meyer, W. 1989 Mesopause temperatures in polar summer. *J. Geophys. Res.*, **94**, 14647.

[113] Weingartner, J. C. and Draine, B. T. 2001 Photoelectric emission from interstellar dust: grain charging and gas heating. *Astrophys. J. Suppl. Ser.* **134**, 263.

[114] Witt, G. 1969 The nature of noctilucent clouds. *Space Res.* **IX**, 157–169.

[115] Woodman, R. F. and Guillen, A. 1974 Radar observations of winds and turbulence in the stratosphere and mesosphere. *J. Atmos. Sci.* **31**, 493–505.

[116] Zeller, O., Zecha, M., Bremer, J., Latteck, R. and Singer, W. 2006 Mean characteristics of mesosphere winter echoes at mid- and high-latitudes. *J. Atmos. Sol. Terr. Phys.* **68**, 1087.

https://doi.org/10.1017/S0022377812000141 Published online by Cambridge University Press